To Improve the Key Properties of Nonlinear Optical Crystal Assembled with Tetrahedral Functional Building Units

Zhiyong Bai,[a,d], Lehui Liu,[a] Dongmei Wang,[a] Chun-Li Hu, *[,b] and Zhoubin Lin[*,a,b,c]

[a]CAS Key Laboratory of Optoelectronic Materials Chemistry and Physics, Fujian Institute of Research on the Structure of Matter, Chinese Academy of Sciences, Fuzhou, Fujian 350002, P. R. China;

[b]State Key Laboratory of Structural Chemistry, Fujian Institute of Research on the Structure of Matter, Chinese Academy of Sciences, Fuzhou, Fujian 350002, P. R. China

[c]Fujian Science & Technology Innovation Laboratory for Optoelectronic Information of China, Fuzhou, Fujian, 350108, P. R. China

[d]University of Chinese Academy of Sciences, Beijing 100049, P. R. China.

Contents of figures and tables

Table S1. Crystal data and structure refinement for ABAF.

Empirical formula	NH_4BAsO_4F
Formula weight	186.77
Temperature/K	293(2)
Crystal system	monoclinic
Space group	Cc
a/Å	4.4453(6)
b/Å	8.1098(10)
c/Å	12.7463(18)
α/°	90
β/°	90
γ/°	90
Volume/$Å^3$	459.51(10)
Z	4
ρ_{calc}g/cm^3	2.700
μ/mm^{-1}	6.663
F(000)	360.0
Crystal size/mm^3	0.13 × 0.12 × 0.09
Radiation	GaKα (λ = 1.3405)
2Θ range for data collection/°	12.074 to 124.438
Index ranges	$-5 \leq h \leq 5$, $-10 \leq k \leq 10$, $-16 \leq l \leq 16$
Reflections collected	3649
Independent reflections	981 [R_{int} = 0.1387, R_{sigma} = 0.0682]
Data/restraints/parameters	981/2/68
Goodness-of-fit on F^2	1.150
Final R indexes [I>=2σ (I)]	R_1 = 0.0617, wR_2 = 0.1549
Final R indexes [all data]	R_1 = 0.0668, wR_2 = 0.1762
Largest diff. peak/hole / e $Å^{-3}$	1.83/-1.35
Flack parameter	-0.04(13)

Table S2. Fractional Atomic Coordinates ($\times 10^4$) and Equivalent Isotropic Displacement Parameters (Å2×103) for ABAF. Ueq is defined as 1/3 of of the trace of the orthogonalised UIJ tensor.

Atom	***x***	***y***	***z***	**U(eq)**
As1	5904(6)	5170.7(15)	6405(3)	12.2(5)
F1	7130(20)	8256(14)	4598(8)	25(2)
O2	8130(20)	8719(15)	6377(9)	17(2)
O3	4230(30)	6901(16)	5908(9)	23(2)
N1	1810(30)	6510(20)	3621(12)	24(3)
O1	3600(30)	9717(13)	5481(11)	19(2)
B1	5810(40)	8390(20)	5582(14)	17(3)
O4	7050(30)	5314(16)	7617(11)	26(3)

Table S3. Anisotropic Displacement Parameters ($Å^2 \times 10^3$) for ABAF. The Anisotropic displacement factor exponent takes the form: $-2\pi^2[h^2a^{*2}U_{11}+2hka^*b^*U_{12}+\ldots]$.

Atom	$\mathbf{U_{11}}$	$\mathbf{U_{22}}$	$\mathbf{U_{33}}$	$\mathbf{U_{23}}$	$\mathbf{U_{13}}$	$\mathbf{U_{12}}$
As1	8.6(7)	13.5(7)	14.4(7)	-1.2(15)	-0.9(5)	-0.9(14)
F1	22(4)	39(6)	15(4)	0(4)	7(3)	-3(4)
O2	14(5)	20(5)	17(5)	2(4)	-2(4)	4(4)
O3	13(5)	28(6)	27(6)	5(5)	-3(4)	1(4)
N1	20(6)	32(8)	21(7)	-1(6)	-2(5)	8(6)
O1	19(6)	13(5)	24(6)	1(4)	3(5)	0(4)
O4	24(6)	29(7)	23(7)	0(5)	-9(5)	-4(5)

Table S4. Selected bond lengths for ABAF.

Atom	Atom	Length/Å	Atom	Atom	Length/Å
As1	O2[1]	1.705(12)	F1	B1	1.391(19)
As1	O3	1.709(12)	O2	B1	1.471(19)
As1	O1[2]	1.721(13)	O3	B1	1.45(2)
As1	O4	1.632(14)	O1	B1	1.46(2)

[1]-1/2+X,-1/2+Y,+Z;[2]1/2+X,-1/2+Y,+Z

Table S5. Selected bond angles for ABAF.

Atom	Atom	Atom	Angle/°	Atom	Atom	Atom	Angle/°
O2[1]	As1	O3	104.2(6)	B1	O1	As1[4]	124.4(11)
O2[1]	As1	O1[2]	110.0(6)	F1	B1	O2	109.7(13)
O3	As1	O1[2]	103.0(6)	F1	B1	O3	113.5(13)
O4	As1	O2[1]	107.2(7)	F1	B1	O1	105.1(13)
O4	As1	O3	115.4(7)	O3	B1	O2	107.1(13)
O4	As1	O1[2]	116.4(7)	O3	B1	O1	108.3(13)
B1	O2	As1[3]	130.5(10)	O1	B1	O2	113.2(13)
B1	O3	As1	125.3(10)				

[1]-1/2+X,-1/2+Y,+Z; [2]1/2+X,-1/2+Y,+Z; [3]1/2+X,1/2+Y,+Z; [4]-1/2+X,1/2+Y,+Z

Table S6. Torsion Angles for ABAF.

A	**B**	**C**	**D**	**Angle/°**	**A**	**B**	**C**	**D**	**Angle/°**
As1[1]	O2	B1	F1	50.6(19)	As1[2]	O1	B1	F1	169.0(10)
As1[1]	O2	B1	O3	174.2(10)	As1[2]	O1	B1	O2	-71.3(16)
As1[1]	O2	B1	O1	-66.4(18)	As1[2]	O1	B1	O3	47.3(17)
As1	O3	B1	F1	79.0(16)	O2[3]	As1	O3	B1	-167.4(12)
As1	O3	B1	O2	-42.2(16)	O1[4]	As1	O3	B1	-52.6(13)
As1	O3	B1	O1	-164.6(11)	O4	As1	O3	B1	75.4(13)

11/2+X,1/2+Y,+Z; 2-1/2+X,1/2+Y,+Z; 3-1/2+X,-1/2+Y,+Z; 41/2+X,-1/2+Y,+Z

Table S7. Hydrogen Atom Coordinates (Å×10^4) and Isotropic Displacement Parameters (Å^2×10^3) for ABAF.

Atom	***x***	***y***	***z***	**U(eq)**
H1A	1950.3	6555.75	2925.42	29
H1B	143.4	5963.55	3797.92	29
H1C	3403.8	5988.15	3880.92	29
H1D	1726	7526.25	3880.92	29

Table S8. Calculated H bonds.

Donor ---H....Acceptor	[ARU]	D – H (Å)	H...A (Å)	D...A (Å)	D - H...A
N1--H1A...O2	[4464.01]	0.89	2.05	2.926(19)	166
N1--H1A...O4	[4464.01]	0.89	2.57	2.88(2)	101
N1--H1B...F1	[1455.01]	0.89	2.51	2.808(18)	100
N1--H1B...O4	[2464.01]	0.89	2.29	2.88(2)	124
N1--H1B...O1	[3445.01]	0.89	2.47	3.13(2)	131
N1--H1C...O4	[2564.01]	0.89	2.52	3.04(2)	118
N1--H1C...F1	[3445.01]	0.89	2.46	2.92(2)	113
N1--H1D...F1	[1455.01]	0.89	2.32	2.808(18)	115
N1--H1D...O4	[4464.01]	0.89	2.38	2.88(2)	115

Translation of ARU-Code to CIF and Equivalent Position Code: [3445.] = [3_445] = -1/2+x,-1/2+y,z; [1455.] = [1_455] = -1+x,y,z; [2464.]= [2_464] = -1+x,1-y,-1/2+z; [2564.] = [2_564] = x,1-y,-1/2+z; [4464.] = [4_464] = -1/2+x,3/2-y,-1/2+z.

Table S9. The summarized average B-O and terminal B-F bond lengths in BO_3F group among selected recently reported NLO crystals which containing BO_3F group.

Crystals	Average B-O bond (Å)	Terminal B-F bond (Å)	Crystals	Average B-O bond (Å)	Terminal B-F bond (Å)
$NH_4B_4O_6F$	1.457	1.410	$Ca_2B_{10}O_{14}F_6$	1.469	1.411
CsB_4O_6F	1.451	1.417		1.468	1.420
RbB_4O_6F	1.457	1.429	$Sr_2B_{10}O_{14}F_6$	1.469	1.396
NaB_4O_6F	1.467	1.408		1.463	1.434
PbB_2O_3F	1.458	1.46	$KBPO_4F$	1.452	1.413
SnB_2O_3F	1.484	1.403	NH_4BPO_4F	1.460	1.387
$SrB_5O_7F_3$	1.470	1.413	$RbBPO_4F$	1.465	1.397
	1.468	1.414	$CsBPO_4F$	1.467	1.404
PbB_5O_8F	1.464	1.390	NH_4BAsO_4F	1.460	1.391

Note: the average B-O bond length is defined as $d_{average}=(d_1+d_2+d_3)/3$, d_1, d_2, and d_3 represent three B-O bond lengths, respectively.

Table S10. The calculated direction and magnitude of ABAF (unit: Debye)

Group	μ_x	μ_y	μ_z	μ (Total)
AsO_4	-1.6545895	0.0637475	-1.21113	2.05148
BO_3F	-0.6871518	0.9463204	-0.06268	1.171165

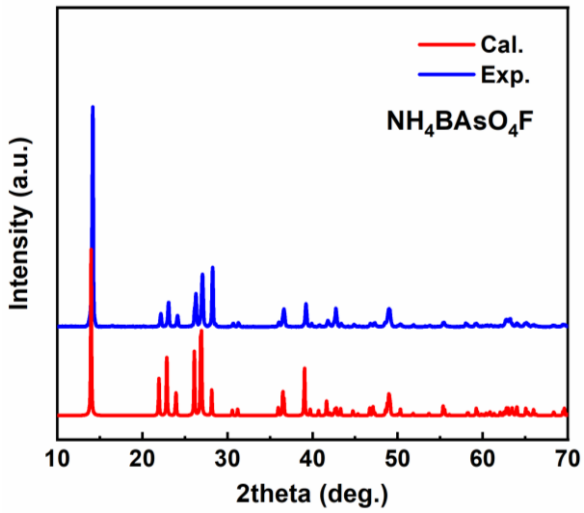

Figure S1. Experimental and calculated powder X-ray patterns of ABAF.

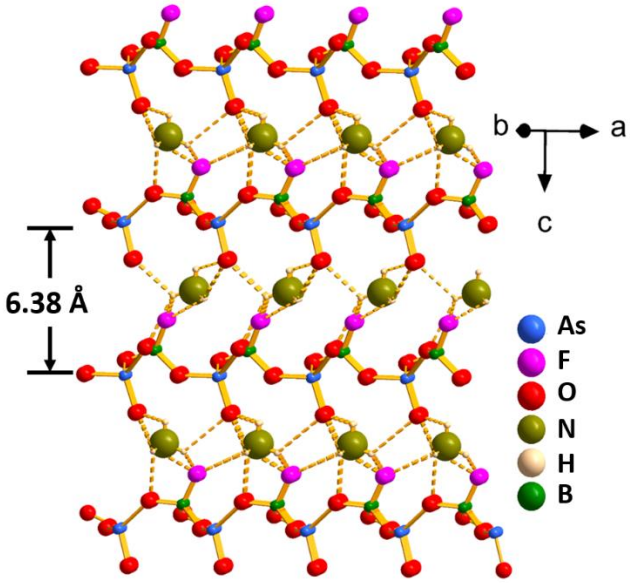

Figure S2. The H-bonds network representation and interlayer distance for ABAF.

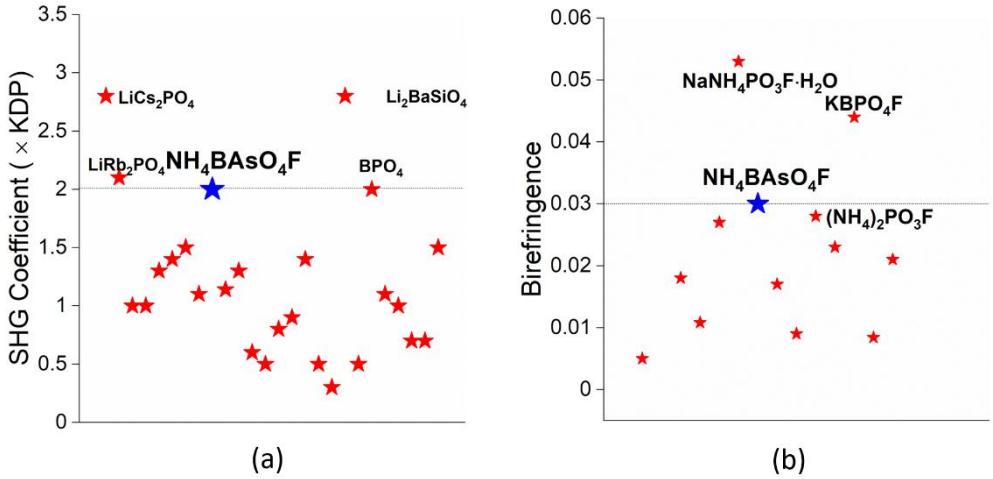

Figure S3. (a) SHG and (b) birefringence scattering plots for nonlinear optical crystals assembled with tetrahedral units.

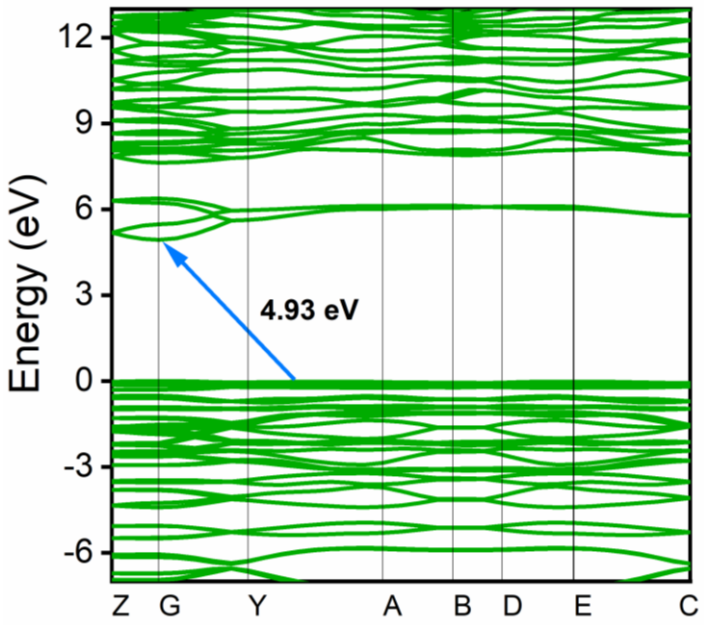

Figure S4. Electric band structures of ABAF.

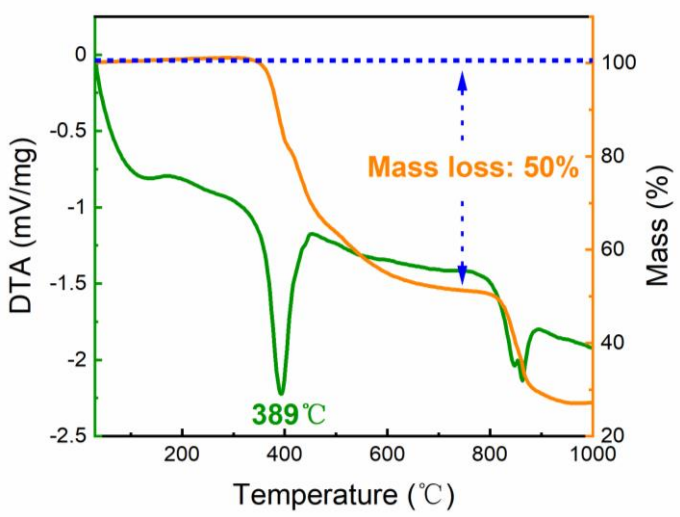

Figure S5. DTA and TG analysis for ABAF.

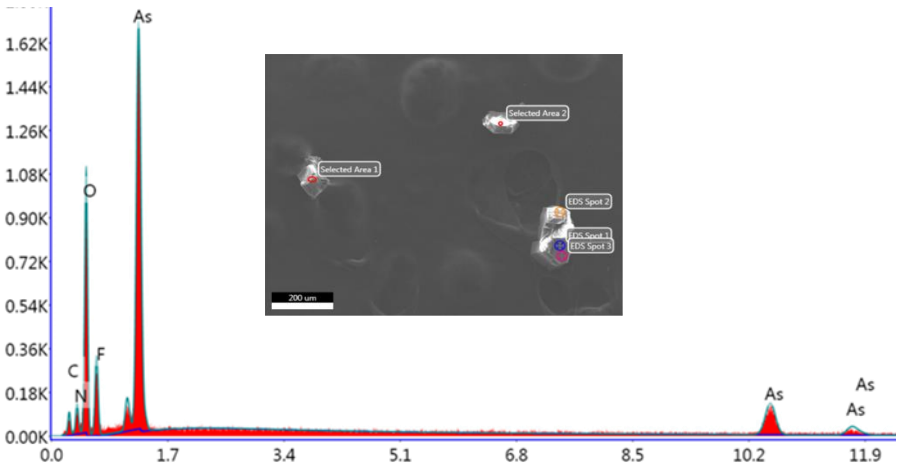

Figure S6. EDS test for ABAF. The element C originates from the base.

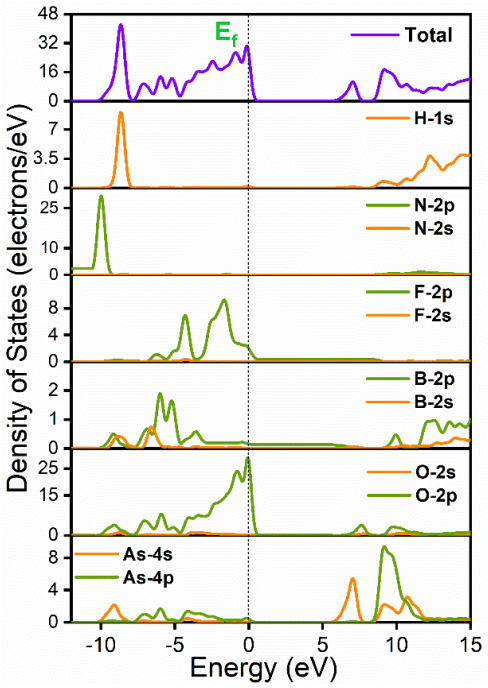

Figure S7. Density of states (DOS) for ABAF.

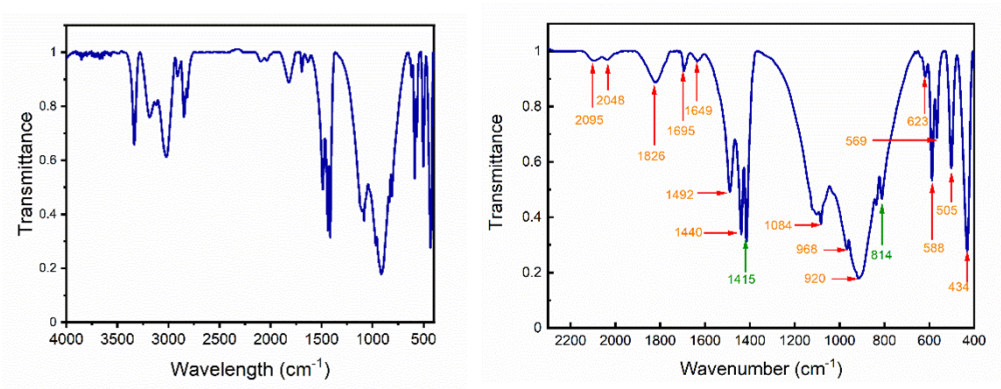

Figure S8. IR spectrum of ABAF. The absorption bands from 3400-1440 are ascribed to vibration of N-H and H bonds. Asymmetric stretching and symmetric out of phase stretching absorption of B-F were found at 1415 cm^{-1} and 814 cm^{-1}, respectively, agreeing well with those of reported (Table S10). The small shift caused by its connectivity with AsO_4 group. The peaks at 968 cm-1 and 920 cm-1 were assigned to the asymmetric stretching vibration and symmetric stretching vibration of As-O in AsO_4, respectively, while the bending vibration absorptions could be observed at 434 and 505 cm^{-1}.

Table S11. Summarized IR absorption peaks of B-F bond in recent reported work.

Compounds	Species	Asymmetric stretching (cm-1)	Symmetric out of phase stretching (cm-1)	Ref.
CsB_4O_6F	BO_3F	1033	806	12
$NH_4B_4O_6F$	BO_3F	1225	798	13
NaB_4O_6F	BO_3F	1236	770	14
PbB_5O_8F	BO_3F	1282	832	15
$SrB_5O_7F_3$	BO_3F	1321	813	16
NH_4BAsO_4F	BO_3F	**1415**	**814**	This work

Experimental Methods.

Synthesis. Chemical reagents KBF_4 (Aladdin, AR, 99%), $NaBF_4$ (Aladdin, AR, 99%), $LiBF_4$ (Aladdin, 98%), NH_4BF_4 (Macklin, 99.99%), H_3BO_3 (SCR, GR), and $NH_4H_2AsO_4$ (Alfa Aesar, 98%) were used as raw materials without further processing. Millimeter-level single crystals of ABAF suitable for single crystal X-ray diffraction were synthesized under a closed system. Specifically, raw materials of H_3BO_3 (6mmol, 0.372g) and $NH_4H_2AsO_4$ (6mmol, 0.954g), and $LiBF_4$ (4mmol, 0.376g) were weighted and then sealed into a 23 mL Teflon-lined autoclave equipped with stainless steel. The autoclave was heated at 230 ℃ in a program temperature controlled oven for 100 h and then cooled down to 130 ℃at a rate of 0.5 ℃/h and eventually cooled down to 30 ℃ in 20 h. The products were washed with deionized water and ethyl alcohol and dried in ~50 ℃. After doing this, millimeter prism-like, colorless, and transparent single crystals were obtained and then been identified as ABAF by powder and single crystal X-ray diffraction techniques without other phases. To obtain large single crystals of ABAF, the different experimental conditions were performed, including the utilization of a variety of raw materials (KBF_4, $NaBF_4$, $LiBF_4$, NH_4HF_2, and HBF_4), ranged reaction temperature (473 K, 503 K) and cooling rate (5, 4, 3, and 0.5 K/h). However, these efforts all failed to obtain large single crystals.

Powder X-ray Diffraction. Powder X-ray diffraction analyses of ABAF were performed at room temperature on a MiniFlex 600 diffractometer equipped with Cu Kα radiation (λ = 1.5406 Å). Data were recorded in the angular range of 2θ = 10-70° with a scan step width of 0.008° and a scan time of 0.5 s. The experimental powder X-ray diffraction patterns are consistent well with those patterns calculated from CIF file.

Sing Crystal X-ray Diffraction. The single crystal X-ray diffraction was performed on a Rigaku ROD, Synergy Custom system, HyPix diffractometer equipped with mirror-monochromatic Ga Kα radiation (λ = 1.3405 Å) at 224 K. A clear, transparent, without cracked single crystal of ABAF was selected under microscope and used for data collection. The data were corrected for the Lorentz factor, polarization, and absorption. By means of Olex2 software, the structure was solved with the SHELXT structure solution program using intrinsic phasing and refined with the SHELXL refinement package using least squares minimization.[1-3] All of the atoms except for B atoms were refined with anisotropic displacement parameters and secondary extinction correction. The Flack parameter is -0.04 (13). The structure was verified by Platon and no higher symmetry was found.[4] Crystallographic data for structural refinements, atoms coordination, thermal parameters, and selected bond lengths, and bond angles are listed in Tables S1-S6.

UV-Vis-NIR Diffuse Reflectance Spectrum. The UV-vis-NIR diffuse reflectance spectrum of ABAF was recorded at room temperature in a PerkinElmer LAMBDA 900 UV-vis-NIR spectrophotometer in the 200-1000 nm wavelength range using $BaSO_4$ as the standard of 100% reflectance. In order to obtain the band gap of ABAF, the diffuse reflectance spectral data were subsequently transferred to the function of reflectance by using Kubelka function:

$$F(R) = \frac{(1-R)^2}{2R} = \frac{K}{S} \qquad (1)$$

where R denotes the reflectance, K the absorption coefficient and S the scattering factor. In the F(R) versus E (eV) plot, extrapolating the linear part of the rising curve to zero provides the onset of the absorption.

SHG Response. According to method proposed by Kurtz and Perry, powder SHG measurements of ABAF were carried out by using 1064 nm coherent light, generated by Q-switched Nd:YAG laser, as incident source. Specifically, polycrystalline samples of ABAF and KH_2PO_4 (KDP) were ground and sieved into distinct particle size ranges (45-58, 58-75, 75-109, 109-150, 150-180, and 180-250 μm). Sieved KDP powder was used as a reference. The intensity of the frequency-doubled output emitted from the sample was collected using a photomultiplier tube.

Thermal Stability Analysis. Differential scanning calorimetry (DTA) and thermogravimetric (TG) analysis of ABAF were performed on a NETZSCH STA 449F3 instrument in a temperature range of 30-1000 °C at a 10 K/min heating rate.

Computation Method. The electronic structures and optical properties were performed using a plane-wave basis set and pseudo-potentials within density functional theory (DFT) implemented in the total-energy code CASTEP.[5-6]For the exchange and correlation function, Perdew-Burke-Ernzerhof in the generalized gradient approximation was chosen.[7] The interactions between the ionic cores and the electrons were described by the norm-conserving pseudopotential.[8] The following valence-electron configurations were considered in the computation: N-$2s^22p^3$, B-$2s^22p^1$, As-$4s^24p^3$, O-$2s^22p^4$, F-$2s^22p^5$ and H-$1s^1$. The number of plane waves included in the basis sets was determined by a cutoff energy of 850 eV. The numerical integration of the Brillouin zone was performed using a Monkhorst-Pack k-point sampling of 6 × 3 × 2. It is worth noting that 192 empty bands were included during the optical property calculations to ensure the accuracy of refractive indices and SHG coefficients. The other parameters and convergent criteria were the default values of the CASTEP code.

The calculation of second-order NLO properties were based on length-gauge formalism within the independent-particle approximation.[9] We adopted the Chen's static formula, which has been derived by Rashkeev et al.[10] and later modified by Chen's group.[11] The static second-order NLO susceptibility can be expressed as

$$\chi^{\alpha\beta\gamma} = \chi^{\alpha\beta\gamma}(\mathrm{VE}) + \chi^{\alpha\beta\gamma}(\mathrm{VH}) + \chi^{\alpha\beta\gamma}(\text{two bands}) \quad (3)$$

where $\chi^{\alpha\beta\gamma}$(VE) and $\chi^{\alpha\beta\gamma}$(VH) give the contributions to $\chi^{\alpha\beta\gamma}$ from virtual-electron processes and virtual-hole processes, respectively; $\chi^{\alpha\beta\gamma}$(two bands) is the contribution to $\chi^{\alpha\beta\gamma}$ from the two-band processes. The formulas for calculating $\chi^{\alpha\beta\gamma}$(VE), $\chi^{\alpha\beta\gamma}$(VH), and $\chi^{\alpha\beta\gamma}$(two bands) are given in ref 5 and 6.

References

1 Dolomanov, O. V.; Bourhis, L. J.; Gildea, R. J.; Howard, J. A. K.; Puschmann, H., *J. Appl. Cryst.*, 2009, **42 (2),** 339-341.

2 Sheldrick, G. M., Acta Crystallogr., *Sect. A: Found. Adv.*, 2014, **7 (1)**, 3-8.

3 Sheldrick, G. M., Acta Crystallogr., *Sect. A: Found. Adv.*, 2015, **71 (1)**, 3-8.

4 L., S. A., *J. Appl. Cryst.*, 2003, **36 (1)**, 7-13.

5 Milman, V.; Winkler, B.; White, J. A.; Pickard, C. J.; Payne, M. C.; Akhmatskaya, E. V.; Nobes, R. H., *Int. J. Quantum Chem.*, 2000, **77 (5)**, 895−910.

6 Segall, M. D.; Lindan, P. J.; Probert, M. A.; Pickard, C. J.; Hasnip, P. J.; Clark, S. J.; & Payne, M. C., *J. Phys.: Condens. Matter*, 2002, **14 (11)**, 2717−2744.

7 Perdew, J. P.; Burke, K.; Ernzerhof, M., *Phys. Rev. Lett.*, 1996, **77 (18)**, 3865−3868.

8 Lin, J. S.; Qteish, A.; Payne, M. C.; Heine, V. V., *Phys. Rev. B*, 1993, **47 (8)**, 4174-4180.

9 Aversa, C.; Sipe, J. E., *Phys. Rev. B*, 1995, **52 (20)**, 14636-14645.
10 Rashkeev, S. N.; Lambrecht, W. R.; Segall, B., *Phys. Rev. B*, 1998, **57 (7)**, 3905-3919.
11 Lin, J.; Lee, M. H.; Liu, Z. P.; Chen, C.; Pickard, C. J., *Phys. Rev. B*, 1999, **60 (19)**, 13380−13389.
12 Wang, X.; Wang, Y.; Zhang, B.; Zhang, F.; Yang, Z.; Pan, S., (2017). *Angew. Chem. Int. Ed. Engl.*, **56(45)**, 14119-14123.
13 Shi, G.; Wang, Y.; Zhang, F.; Zhang, B.; Yang, Z.; Pan, S.; Poeppelmeier, K. R. *J. Am. Chem. Soc.*, **139(31)**, 10645-10648.
14 Zhang, Z.; Wang, Y.; Zhang, B.; Yang, Z.; Pan, S., *Angew. Chem. Int. Ed. Engl.*, **57(22)**, 6577-6581.
15 Mutailipu, M.; Zhang, M.; Zhang, B.; Yang, Z.; Pan, S., *Chem. Commun.*, **54(49)**, 6308-6311.
16 Mutailipu, M.; Zhang, M.; Zhang, B.; Wang, L.; Yang, Z.; Zhou, X.; Pan, S., *Angew. Chem. Int. Ed. Engl.*,**130(21)**, 6203-6207.